Engineering the Breaking of Topological Protection in Valley Photonic Crystals Enables to Design Chip Level Functions for THz 6G Communications and Beyond

Abdu Subahan Mohammed, Gaëtan Lévêque, Edouard Lebouvier, Yan Pennec, Marc Faucher, Alberto Amo, Pascal Szriftgiser, and Guillaume Ducournau, *Member, IEEE*

***Abstract*—The realization of integrated, low-loss, and efficient systems for data-intensive applications such as augmented and virtual reality requires on-chip integrated photonic circuits, which have great potential for advanced information and communication technologies, including 6G wireless networks and intra- and inter-chip communication systems. A promising platform for achieving this revolution is Valley Photonic Crystals (VPCs). VPCs enable the construction of topological interfaces, which facilitate the propagation of light with minimal losses and backscattering through unidirectional edge modes. Interfacial topological interfaces and the degree of topological protection experienced by these robust edge modes is a relatively new perspective worth exploring. The ever-increasing demand for faster data rates in data-intensive applications like augmented and virtual reality necessitates the exploration of frequencies beyond the conventional 300 GHz band. In this study, we introduce variations in topological protection by considering different interfacial designs and suitable air-hole geometries for passive functional devices. We show that the partial breakup of topological protection can be an asset for the design of on-chip passive functionalities. We focus on bearded and zigzag junctions and appropriate air hole geometries for VPC unit cells. To experimentally verify the scalability of topological protection, we demonstrate the performance of terahertz (THz) topological ring resonators and THz double cavity resonators designed for operation in the 600 GHz frequency region. This work showcases how the scaling of topological protection can be achieved by utilizing a combination of air hole geometry and interfacial degrees of freedom, providing functional tuning of devices at the chip level.**

***Index Terms*—Terahertz, topological photonics, waveguides.**

Manuscript received 25 March 2024; revised 5 June 2024; accepted 23 June 2024. Date of publication 5 July 2024; date of current version 2 December 2024. This work was supported in part by the France 2030 programs, PEPR (Programmes et Equipements Prioritaires pour la Recherche), CPER Wavetech, in part by the TERAOPTICS programs and in part by the National Institute of Information and Communications Technology (NICT) through Beyond 5G R&D Promotion Program under Grant 00901. The PEPR is operated by the Agence Nationale de la Recherche (ANR), under Grant ANR-22-PEEL-0006 (FUNTERA, PEPR 'Electronics') and Grant ANR-22-PEFT-0006 (NF-SYSTERA, PEPR 5G and beyond - Future Networks). The Contrat de Plan Etat-Region (CPER) WaveTech was supported in part by the Ministry of Higher Education and Research, the Hauts-de-France Regional council, the Lille European Metropolis (MEL), in part by the Institute of Physics of the French National Centre for Scientific Research (CNRS), and in part by the European Regional Development Fund (ERDF). The TERAOPTICS project was supported by the European Union's Horizon 2020 Research and Innovation Programme under the Marie Skłodowska-Curie Grant Agreement number 956857. The nanofabrication work was supported in part by the French RENATECH network, in part by the Equipex+ Nanofutur operated by the ANR under Grant IA-21-ESRE-0012. The characterization work was supported by the Equipex+ ADD4P under Grant IA-21-ESRE-0007 and the design work was supported by the European Research Council under EmergenTopo Grant 865151. This work was also supported in part by French Government through the Programme Investissement d'Avenir (I-SITE ULNE /ANR-16-IDEX-0004 ULNE) managed by the Agence Nationale de la Recherche, in part by the Labex CEMPI under Grant ANR-11-LABX-0007, and in part by the region Hauts-de-France. *(Corresponding author: Guillaume Ducournau.)*

Abdu Subahan Mohammed, Gaëtan Lévêque, Edouard Lebouvier, Yan Pennec, Marc Faucher, and Guillaume Ducournau are with the CNRS, Centrale Lille, University Polytechnique Hauts-de-France, UMR 8520-IEMN, Institut d'Electronique de Microélectronique et de Nanotechnologie, Université de Lille, F-59000 Lille, France (e-mail: guillaume.ducournau@univ-lille.fr).

Alberto Amo and Pascal Szriftgiser are with the CNRS, UMR 8523 – PhLAM, Laboratoire de Physique des Lasers, Atomes et Molécules, Université de Lille, F-59000 Lille, France.

Color versions of one or more figures in this article are available at https://doi.org/10.1109/JLT.2024.3423659.

Digital Object Identifier 10.1109/JLT.2024.3423659

I. Introduction

TOPOLOGICAL photonics has gained significant attention in recent years due to its unique properties and potential applications [1], [2], [3], [4], [5]. Extensive studies have been conducted on various systems including photonic crystals [1], [6] metamaterials [7], [8] Weyl semimetals [9], and nonlinear systems [10], [11]. Among them, photonic crystals are a promising platform for creating photonic analogs of topological quantum systems [12], such as the quantum Hall effect [13], quantum spin Hall effect [14], and quantum valley Hall effect [15], [16]. This can be achieved by breaking time-reversal or spatial inversion symmetry in different photonic crystal structures, leading to scalable and robust topological effects at various frequency regimes [17]. Besides the topologically protected edge waves that occur at the interface between two photonic topological insulators (PTIs) possess exceptional properties such as robustness, defect immunity, backscattering suppression, and unidirectional transmission [1]. Significant efforts have been directed towards investigating spin-Hall PTIs [18], [19], [20], [21], [22] and valley-Hall PTIs, also known as valley-Hall photonic crystals or VPCs [23], [24]. These PTIs exhibit time-reversal symmetry and do not require magnetic components or temporal modulation. They have already shown promising potential for use in modern optical devices, such as reflectionless waveguides [2], topological quantum interfaces [25], topological light

sources [26], topological lasers [27], [28], topological splitters [21] and robust delay lines [29]. However, experimental studies on PTIs have thus far been mostly limited to microwave [2], [17], [21], [22], [23], [30] and optical frequencies [1], [18], [24], [25].

The progress of PTI experiments in THz has been constrained due to the technological immaturities imposed by the currently available material platforms and tools for characterization in the THz. The THz band extended from 0.1 THz to 10 THz and a wavelength of 0.03–3 mm, which bridges the gap between microwaves and optical waves. Also, this region is known as the 'THz gap' owing to the lack of many functional devices in this frequency range [31]. Despite the current technological immaturity of the THz band, its unique frequency range has garnered significant attention among researchers in recent years due to its diverse and promising potential applications in sensing [32], imaging [33], [34], and high-speed data communications [35]. Developing THz technology can be an efficient solution for futuristic and data-hungry technologies like virtual reality, augmented reality, and holographic communications [31], [36], [37]. THz technology is expected to be the critical catalyst for 6G communication networks, enabling wireless data transfer in terabits per second over kilometers. Mastering the THz transmission relies on the tremendous hurdles that must be tackled regarding the sources, detectors, photonic integrated circuits, and antenna technology. Extremely small on-chip photonic integrated circuit systems, which enable high-speed terabits per second data transfer, gain importance due to the high demand for compact devices for THz technology. The conventional THz metallic interconnects are highly lossy and rely on voluminous bulky systems that can only transfer limited bandwidth [38]. Key steps towards on-chip THz communication and signal processing required building low-loss, low-cost, low-dispersion, integration-compatible efficient photonic waveguides and components that are highly robust to defects and sharp bends.

Silicon-based Valley-Hall PTIs have already demonstrated their efficiency in constructing passive devices within the THz region, primarily due to their ease of fabrication and the simplicity of their designs [40], [41], [42], [43]. A quantum cascade laser in this configuration was also reported [27]. Even if most of these initial demonstrations sit in the 300 GHz range, the next research window is definitively in the sub-millimeter range. Potentialities of new topological photonics approaches, while being pulled forward thanks to the next-wireless region 300 GHz-(H band), need to be investigated at higher frequencies. Obviously, operating at higher THz frequencies offers more bandwidth, enabling high-speed data transfer with simple and less complex modulation techniques like PAM (Pulse Amplitude Modulation), QAM16 (Quadrature Amplitude Modulation) and QPSK (Quadrature Phase Shift Keying), etc. [39].

In topology designs based on VPC, the photonic bandgap is created by introducing asymmetrical air holes in the VPC unit cell, which breaks inversion symmetry. The reason for the minimal loss of propagation and bending in VPC waveguides is the presence of topologically protected edge states that exist due to the bulk VPC on both sides of the interface.

Furthermore, the linear dispersion of topological edge states observed in VPC waveguides offers the advantage of utilizing the entire bandwidth for on-chip communication, while keeping signal delay to a minimum across various frequencies [40], [41].

Most of existing reports have explored the geometrical optimization of air holes in VPCs [42], [43], as well as the design of composite interface junctions for air-slot-like VPC waveguides with 60° bends and unchanging bearded interfaces to enable topologically protected propagation of THz waves over a 20% relative bandwidth [44]. There remains a gap in our understanding regarding a comprehensive formula for scaling topological protection utilizing these degrees of freedom. Notably, a study has demonstrated that bearded-stack VPCs with glide-plane symmetry exhibit higher uni-directional coupling efficiency compared to zigzag-stack VPCs with inversion symmetry [45]. While specific applications have been investigated with optimizations of air hole geometry and interfacial topological studies, a broader exploration of a general formula to effectively enhance topological protection for a wide range of futuristic applications remains unexplored. Moreover, perfect topological protection can be detrimental for some applications such as photonic crystal resonant cavities and add-drop filters. In these cases, perfect protection results in the absence of any resonant feature, and the controlled breakup of topological protection can be an asset to optimize some functionalities [46]. This significant knowledge gap necessitates further investigation and presents an opportunity for impactful scientific contributions.

Ring resonators are diverse functional devices and a crucial ingredient of integrated photonic circuits as they can act as filters, sensors, and delay lines, and as a means of enhancing nonlinear optical effects [47]. By leveraging the topological channel designs [48], [49], [50], photonic structures emulating the basic functions of conventional ring resonators have also been proposed recently [51], [52], [53], leading to superior devices with improved reliability. A few demonstrations have reported topological photonic ring resonators with high Q-factor, utilizing VPCs. These demonstrations have shown a robust Q-factor as high as 679 [54], 1210 [52], and 20000 [54]. These resonators find applications in quantum photonic chips, notch, and filters at different frequencies [51], [52], [56]. Recently, silicon-based photonic crystal structures have been in high demand for implementing high-Q compact cavities used for sensing applications [56], [57]. Furthermore, silicon-based integrated circuits can be fabricated using a single etching process and are compatible with the industrial-grade complementary metal-oxide semiconductor (CMOS) fabrication technology. On the other hand, silicon photonics [59], [60], [61], [62] has already become a mature technology with a wide range of passive functions like waveguides, filters, multiplexers, modulators, and photodetectors, enabling cost and energy efficiency for data-driven applications [63], [64]. Silicon-on-insulator (SOI) offers a platform to fasten and enhance the data transfer within and between the silicon chips by using optical counterparts to their electronic components.

The unique response of topological ring resonator systems has the potential to be utilized for the development of highly compact and efficient sensors, optical switches, filters, and quantum information processing at THz frequencies. Additionally, the use of topologically protected high Q-resonators could open up new avenues for nonlinear technologies in the THz frequency

domain. However, despite their potential applications, there is still a significant lack of research regarding topological photonic crystals at THz frequencies, which hinders their practical realization [43]. A numerical study on the effects of defect states in THz topological ring resonators has already been explored [65] and few relevant studies have been reported in THz valley photonic crystal-based waveguides and devices which is essentially a promise towards THz integrated topological photonics [40], [41], [44], [66], [67], [68], [69], [70], [71], [72], [73], [74].

Our study provides clear evidence of being able to enhance or partially break up topological protection by utilizing different interface geometries in distinct topologically classified valley photonic crystals. These interface geometries include bearded and zigzag terminations. In particular, we compare topological protection in photonic crystals made of triangular and circular holes. We focus on designing THz topological ring resonators with single cavities and a double cavity design. Furthermore, our work is the first experimental achievement of functional THz topological devices operating in the 600 GHz region.

The article is organized as follows. Section II is devoted to a general presentation of the VPC geometrical structure based either on triangular or circular air holes in a silicon substrate together with their band diagram and Berry curvature simulations. In Section III, to evaluate edge topological protection, the transmission coefficient through a triangular resonator is numerically calculated for 2D and 3D systems. By changing the shape (triangular or circular) of holes and the type (bearded or zigzag) of the interface, we evidence that the quality of the topological protection varies significantly, which can be used to tune the quality factor of terahertz filters. Section IV reports experimental results in the 600 GHz range on fabricated samples, where transmission measurements performed with vector network analyzer (VNA) are in very good agreement with simulations.

Fine-tuning of the design allows the VPC chip resonator to display high topological protection and quasi-immunity to backscattering, simultaneously with flat group delay. Conversely, other configuration yields sharp resonances with a high Q factor. To show the potentiality for applications, Section V reports the transmission spectrum and group delay for a double-cavity resonator. Unlike the single cavity resonator which exhibits flat transmission, sharp resonances are also observed in good agreement with the numerical simulations.

II. Valley Photonic Crystals

A. Design and Fabrication

In this work, topological device chips are prepared on Silicon-on Insulator (SOI) wafers with 90 μm-thick high-resistivity silicon (HR-Si) of resistivity larger than 10 kΩ-cm and relative permittivity 11.7. HR-Si offers a CMOS-compatible platform with low absorption loss and a non-dispersive refractive index. Here, the VPC device layer is initially asymmetrically placed between the SiO_2 substrate and top air region from the configuration of the initial wafer used. However, during the fabrication process, the Si region below the SiO_2 is fully etched then the only remaining part is the 90 μm HR-SI, and the VPC device layer suspended over the air. Fig. 1 presents the schematics of two topologically distinct Si-VPC designs, composed of a well-known graphene-like honeycomb lattice with equilateral triangular or circular air holes. Here we assign a zigzag interface (zz) for the triangular hole design and a bearded interface (bd) for the circular holes. For 3D simulations of the devices, lattice constants are $a_1 = 137$ μm and $a_2 = 126$ μm (see Table I). For 2D simulations, in order to set the first gap at 600 GHz, lattice constant values have been adjusted to respectively $a_1 \sim 113$ μm and $a_2 \sim 108$ μm, see Table II.

TABLE I
Membranal Photonic Crystals Geometrical Parameters

Holes	Period (μm)	d_1 (μm)	d_2 (μm)
Triangular	137	89	48
Circular	126	54	18

TABLE II
Bidimensional Photonic Crystals Geometrical Parameters

Holes	Period (μm)	d_1 (μm)	d_2 (μm)	d_0 (μm) Equal size
Triangular	~113	0.65 a_1 74	0.35 a_1 40	0.50 a_1 57
Circular	~108	51	17	34

Note: compared to the membrane case, it is known that frequencies are lower. In order to set the gap at 600 Ghz the periodicity values of a_1 and a_2 have been adjusted.

Fig. 1(a) and (b) shows the schematics of two topologically distinct Si-VPC designs. Fig. 1(a) comprises two oppositely facing inverted equilateral triangular holes with a side length of $d_1 = 74$ μm and $d_2 = 40$ μm (rhombus-shaped shaded region in Fig. 1(a). The triangles are leveled off 10 micrometers before the vertex to reduce defects during the deep etching of the device). Similarly, each VPC unit cell in Fig. 1(b) comprises two circular air holes with a diameter of $d_1 = 51$ μm and $d_2 = 17$ μm. For the triangular holed unit cell design, when the triangular holes have equal size $d_0 = (d_1+d_2)/2 = 0.5\ a_1 = 57\mu$m, the unit cell shows C_6 rotation symmetry that leads to a pair of degenerate Dirac points (at the K_0 and K_1 valleys) in the band as shown in Fig. 1(c).

Upon breaking the C_6 rotation symmetry to C_3 rotation symmetry by setting $d_1 \neq d_2$ (in our case ($d_1 = 0.65\ a_1$ and $d_2 = 0.35\ a_1$), inversion symmetry is broken and leads to a bandgap (0.57 THz $< f <$ 0.64 THz, see red lines in Fig. 1(c)). A similar situation takes place for the VPCs with circular holes shown in Fig. 1(b) and (d). In this case the lattice period is $a_2 = 108$ μm, the larger circle diameter $d_1 = 51$ μm, the smaller circle diameter $d_2 = 17$ μm and $d_0 = (d_1+d_2)/2 = 34$ μm. Here also band gap opens at the same frequency range when inversion symmetry is broken. It is well established that VPCs exhibit non-zero Berry curvatures localized at the K_0 and K_1 valleys. To quantify these Berry curvatures, we employed a plane wave expansion method implemented in MATLAB. The topological interfaces appear when using to VPC with opposite valley Chern

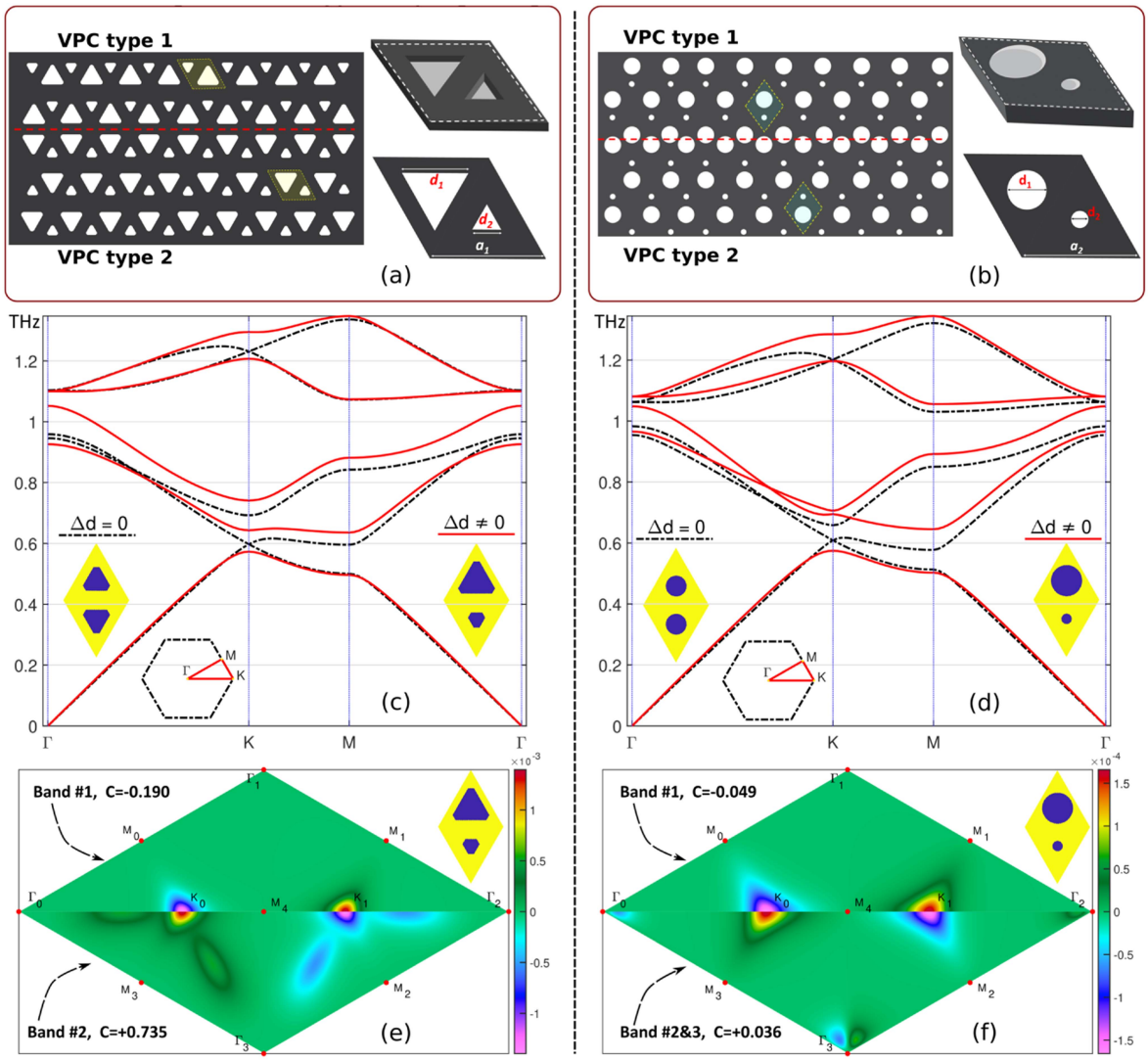

Fig. 1. (a, c, e) on the left: triangular holes structure. (b, d, f) on the right: circular holes structure. (a, b): Schematic representation of the fabricated sample. The yellow-shaded regions show unit cells. Magnified view of the unit cell in 3D before leveling of corners and in 2D after leveling off are presented at right side of the images. See Figs. 7 and 8 for images of actual samples. The red dashed lines indicate the zigzag interface. (c, d): Band diagrams with and without inversion symmetry used in bidimensional simulations. (e, f): Berry simulation curvatures (TE polarization) near the K and K′ valleys. In the case of circular holes, band 2 and 3 are degenerated, the Berry curvature calculation must be performed for both of them. Valley Chern number (C) are given for the half-left side (Γ0Γ1Γ2) of the diagram.

index. The computational analysis confirms the presence of non-zero Berry curvatures around distinct valleys, as depicted in Fig. 1(e) and (f). Furthermore, it is noteworthy that within the same band, these Berry curvatures are identical in magnitude but possess opposite signs for the K_0 and K_1 valleys. Consequently, the net integrated Berry curvature associated with any single band is zero. This phenomenon is additionally underpinned by the preservation of time-reversal symmetry within the VPC structure.

III. Numerical Simulations

To analyze the degree of topological protection of the considered designs we perform finite element simulations of the electromagnetic field inside the structures. All simulations have been done using the software COMSOL Multiphysics. We will see that different hole geometries and types of topological edges can show variations in the quality of their topological protection. Indeed, an edge mode can experience conversion into the mode with opposite pseudo-spin at different locations all along a device, through back-scattering at splitters and abrupt bifurcations, or transmission along topologically forbidden directions across splitters. THz topological ring resonators, addressed at their tip though a linear topological waveguide, allows enhancing the effect of small ruptures of topological protection through the recirculation of the mode inside the cavity, which manifest themselves as sharp minima in their transmission spectra. On the contrary, if topological protection is perfect, the electromagnetic wave cannot be reflected towards the source, the reflection coefficient is then zero and the transmission coefficient must be unity for any frequency at which the edge-mode exists.

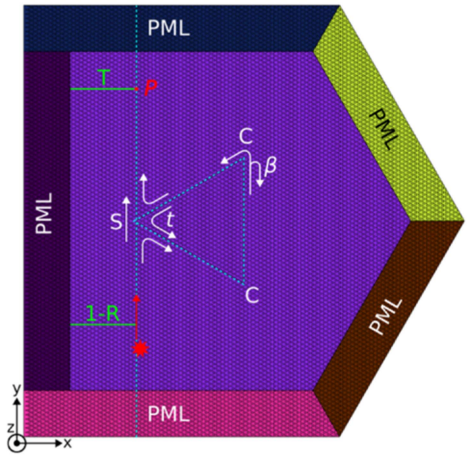

Fig. 2. Numerical setup for finite elements simulations. PML indicate the domains or Perfectly Matched Layers; transmission (T) and reflexion (R) are computed along the corresponding the green lines. The star indicates the location of the source. Parameters t and β indicate respectively the inter-cavity transmission coefficient at the splitter S, and the back-scattering coefficient at a corner C, both in amplitude of the edge-mode.

A. *Bidimensional Simulations*

We first start by investigating bidimensional topological circuits, based on either circular or triangular air holes in a silicon matrix (lossless and with dielectric constant $\varepsilon_r = 11.7$), where light is guided along either zigzag or bearded interfaces. The triangle's corners have been cut off at a length of 10 μm, to ease the fabrication process as shown in Fig. 1(c). In all configurations, the interface is realized between large circular or triangular holes as shown for example in Fig. 1(a) and (b) for the 3D case. Further details about the typical numerical setup is given on Fig. 2, illustrating the case of a THz topological triangular ring resonator with a bearded edge (underlined by cyan dashed lines) and triangular holes corresponding the Fig. 3(a).

The simulation domain is surrounded by Perfectly Matched Layers that absorb outgoing waves to simulate an infinite system. The main elements of the simulations are indicated on Fig. 3(a). The source is a circularly polarized dipole located at the red star. Its spin depends on the geometry of the edge. The transmission (T) and reflection (R) power coefficients are evaluated by integrating the Poynting vector's y-component through their corresponding propagation direction (dashed line in Fig. 3(a)) and normalizing to the power of the edge mode propagating along a straight edge excited by the same source.

We consider TE polarization: the electric field is parallel to the plane *xy* of the lattice, and only the *z* component H_z of the magnetic field is non-zero. All THz topological ring resonators in this section have a side length equal to 28 lattice periods.

In order to match the frequency position and width of the band gap of the device, the geometrical parameters had to be slightly adjusted in the bidimensional geometry. This does not change the general observations and conclusions of the corresponding simulations.

We have simulated the dispersion diagrams, transmission coefficient T and associated group delay τ_g ($\tau_g = -d\varphi/d\omega$, evaluated from the phase φ of the component H_z of the magnetic field at point P on Fig. 3(a)) for the four possible combinations between hole shapes (triangular or circular) and interface types (zigzag or bearded). Fig. 3(b)–(g) shows the corresponding dispersion diagrams of the edge modes for circular (b), triangular (e) holes, where the bearded (bd) edge mode is plotted in red, and the zigzag (zz) edge mode is in blue, while the blue-green areas indicate the bulk modes. Transmission coefficient and group delay are shown for (c), triangular holes and zigzag edge, (d), triangular holes and bearded edges, (f), circular holes and zigzag edge, and (g), circular holes and bearded edge. The geometrical parameters of the lattices are given on Table II. Regardless the type of hole, shapes of the transmission spectra clearly evidence that zigzag edges (c,f) better preserve the topological protection than bearded edges (d,g). That can be clearly seen from the number of observable narrow resonances in the computed spectra, which is larger for bearded than for zigzag interfaces, both for triangular and circular holes. Recall that the transmission through the triangular resonant ring should not show any resonant feature in case of perfect topological protection. The transmission resonance peaks visible in particular in Fig. 3(d), (f), and (g) evidence deviations from perfect topological protection. For zigzag edges (Fig. 3(c) and (f)), transmission minima occur only for the lowest frequencies within the band-gap, and never reach zero. For triangular holes (Fig. 3(c)), the transmission reaches its lowest value of 91% at F = 570 GHz, and stays very close to 1 otherwise. Resonances of the structure are however clearly visible in the frequency dependence of the group delay, which presents a regular pattern of Lorentzian-type resonances throughout the whole frequency window, with lowest amplitude close to 600 GHz. Indeed, despite not being redirected toward the source, the edge mode is reinjected at the splitter after each tour (coefficient t on Fig. 3(a)) inside the triangular resonator: this mode spends more time and is then enhanced inside the cavity, which correlates with the enhanced group delay. For circular holes (Fig. 3(f)), resonances appear again in the low-frequency part of the band gap (F<580 GHz) and reach 18% at F = 570 GHz. The small oscillation in T is related to a small reflection on the PMLs, which leads to a weak Fabry-Perot effect between PMLs at the top and the bottom of the simulation domain. Again, the group delay is periodically enhanced but decreases in amplitude with frequency.

For the bearded edge, Fig. 3(d), more transmission minima are visible, however, the resonances are noticeable only for frequencies lower than 585 GHz, where a minimum of 12% is reached at F = 582.6 GHz. The behavior of the group delay is similar to Fig. 3(c), but the minimum is reached close to 620 GHz. Finally, the combination of bearded edge with circular holes, Fig. 3(g), appears to be the one where the loss of topological protection is the largest, as a regular series of sharp resonances reaching 0 (except for F = 606 GHz) is obtained in the whole range of simulated frequencies. Most of the resonances appear as split-resonances, which relate to the interference between the edge modes traveling in the direct and indirect orientations along

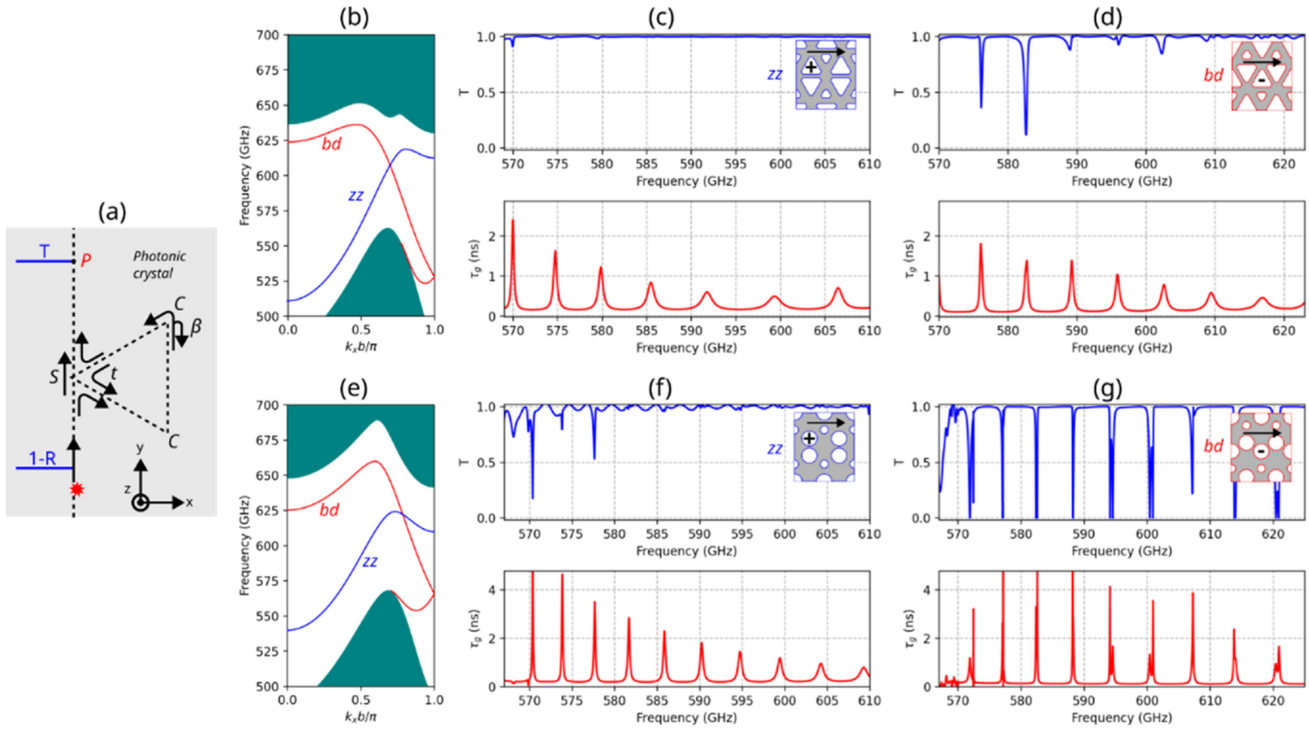

Fig. 3. (a) Diagram indicating the main elements of the simulation. Corners are labelled C, the splitter S. Parameters t and β indicate respectively the inter-cavity transmission coefficient at the splitter S, and the back-scattering coefficient at a corner C, both in amplitude of the edge-mode. (b, e) Dispersion diagrams, transmission spectra T (top) and group delay τ_g (bottom) computed through resonators in photonics crystals with triangular (c, d) or circular (f, g) holes, for bearded (c, f) or zigzag (d, g) interfaces. On the dispersion diagrams (b, e), blue-green areas indicate the bulk modes of the lattice, the blue (resp. red) curve is for the bearded (resp. zigzag) interface. The position and spin of the source is indicated in the insets showing the shape of the edge by a +/- sign for spin up/down polarization. The arrows show the direction of the energy flow.

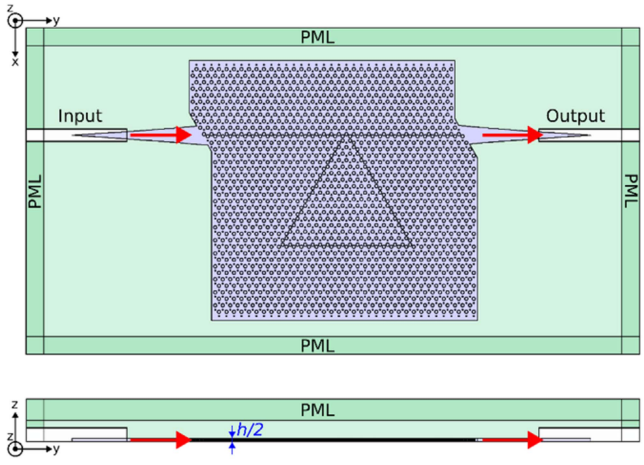

Fig. 4. Numerical setup for finite elements simulations of the full membranal device. The thickness of the membrane is h = 90μm, the dielectric constant of silicon is 11.7.

the triangular resonator. As shown in [46], those back-reflections are mostly due to reflections of the edge modes at the corners of the cavity, with weaker contributions from the splitter. The largest double-peak splitting is obtained for resonances close to F = 600 GHz and F = 594 GHz, with separations of ΔF = 0.43 GHz and ΔF = 0.48 GHz respectively. From the value of splitting and following the method described in [46], we can estimate the back reflection at each corner of the triangular resonator to be $|\beta|^2 = 2.3\%$ in power. It can be mentioned that the group delay is always positive, and splits in double peaks as for the transmission coefficient. Overall, the group delay is larger than 2 ns at resonances, which is about twice as large as the value obtained for the bearded edge with triangular holes. The group velocity v_g of the edge mode can be evaluated from the dispersion curve, which leads to a value of $v_g = 0.2c_0$ for F = 597 GHz, where c_0 is the velocity of light in a vacuum. Owing to the size of the cavity, it appears that the edge mode takes about 0.2 ns to make one tour of the cavity, which indicates that it travels between 5 and 20 tours at resonances before being out-coupled. Fig. 5 shows typical field distributions for a highly transmitted frequency (a) and at a resonant minimum (b).

The main conclusions from these simulations are: (i) zigzag interfaces are more topologically robust than bearded ones as previously discussed when studying photonic crystals at telecom wavelengths [45]; (ii) for both types of edges, circular holes show more and deeper transmission resonances than triangular holes, pointing to a poorer protection than triangular holes.

B. 3D Simulations

The exact three-dimension of the devices have been simulated using Comsol after direct importation of the gds (layout) files used for the fabrication. The typical numerical setup is shown in Fig. 4.

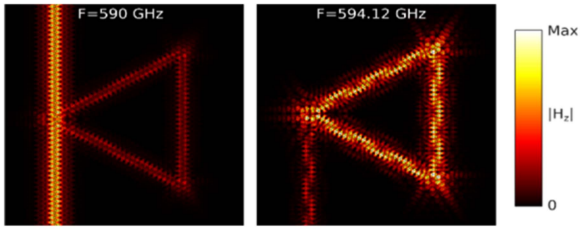

(a) (b)

Fig. 5. Topological ring resonator: magnetic field distributions corresponding to the spectra presented in Fig. 3, specifically for the panel (f) correspond to circular holes with zigzag edges (a) Transmission at 590 GHz, away from any resonance. (b) Transmission at 594.12 GHz.

The device is fed by a waveguide whose dimensions are the same as in the experiments, ie 500–750 GHz metallic hollow-core waveguide. The transmission is computed through an output waveguide with identical characteristics. Only half of the membrane is modelled, and a symmetry plane is applied on the bottom surface (parallel to *xy*) of the simulation domain to compute symmetric modes: the magnetic field is perpendicular to that plane. In all the following simulations, a small oscillation is observed in the transmission spectra, related to reflections of the edge modes on the limits of the photonic crystal. The geometrical parameters of the lattice are given in Table I. In this section, the side length of the THz topological ring resonators is equal to 16 lattice periods.

Fig. 6 shows the numerical results for the devices with single-cavities resonators. Only two types of topological interfaces have been simulated which, within the four geometries discussed above, should correspond, to the highest degree of topological protection (triangular holes and zigzag interface, Fig. 6(a)) and the lowest protection (circular holes and bearded interface, Fig. 6(b)). In each case, band diagrams picturing the corresponding dispersion curve have been plotted, where the grey area represents the light cone, and the green surface indicates the bidimensional continuum of the lattice bulk modes. Both bidimensional (see Fig. 3) and 3D-simulated edge modes have similar dispersion relations (except for the presence of the light cone).

For the purpose of experimental verification, we have specifically focused on fabricating these two types of designs that represent high and low levels of topological protection. These selected designs serve as examples to showcase the range of possibilities and demonstrate the influence of topological protection on device performance. As for the bidimensional case, the transmission curve for triangular holes and zigzag interface, Fig. 6(a), does not show noticeable resonance features, which implies that the amount of backscattering related to the loss of topological protection is negligible. However, cavity resonances are still observable in the group delay, which presents, as for the bidimensional case, a series of regularly spaced positive maxima, with amplitude reaching a minimum close to F = 595 GHz. Sharp and deep transmission resonances are obtained for circular holes and bearded interface, Fig. 6(b), with four clear double peaks at F = 576, 592, and 600 GHz. The frequency interval of the two split-resonances at 592 and 600 GHz are respectively $\Delta F = 0.49$ and 0.51 GHz. Following the same procedure as for the bidimensional case, we estimate a backscattering coefficient at the corners to be 1.7% in power. The most striking difference with Fig. 3 is the shape of the group delay, which takes negative values (down to –5 ns) at each transmission minima of the two mentioned split-resonances, where it always keeps positive values in the bi-dimensional simulations. The reason is the shorter size of the lattice in the membrane (3D) system, related to numerical and fabrication constraints: at resonances, the field is enhanced inside the cavity and leaks in the air along the edges of the device. This introduces an anomalous evolution of the phase which results in negative group delays.

IV. Experimental Results

A. Sample Fabrication

To experimentally verify the proposed THz topological ring resonator designs and demonstrate topological scaling for functional tuning of the resonator using the two interface domains designs, we fabricated the photonic crystal devices using SOI wafers. Such an approach was already reported for 600 GHz-band membrane-based waveguides [75]. Silicon wafers are the most advanced starting material for wafer-based microfabrication. The wafer we used include a 90-um device layer on 2 um buried oxide and thick silicon handle in the bottom. The fabrication is based on photolithography, followed by deep reactive ion etching (DRIE) implementing a Bosch-process recipe developed for our design. SEM images for etched holes are shown in Figs. 7 and 8. The lattice constant and diameters of the air holes of the VPCs are designed appropriately with the parameters mentioned in table S2. In order to streamline the fabrication and etching processes, we have implemented a modification in our design of usual triangular holes, the triangles are levelled off 10 micrometers before the vertex. This adjustment has been made to ease the etching procedure, ensuring more precise and straightforward fabrication of the devices. This was also considered and implemented in the designs for simulations. To facilitate the light coupling into and out of the topological resonator injection waveguides with tapered widths (Figs. 7 and 8) are designed at the two ends of the topological waveguide.

B. Characterization Testbed

Transmission and dispersion estimation are based on measurements obtained by a vector network analyzer (VNA) coupled to frequency extenders. The VNA measurement was achieved from 500–750 GHz (WR1.5). In this case, the VNA was waveguide-calibrated using a set of waveguide Thru / Reflect / Match standards (TRM calibration procedure), for WR 1.5. This hollow waveguide attached to VNA extenders is compatible with the coupler dimensions of the Si-VPC chip, which were used to in-couple/out-couple the signal to/from the Si-VPC. The waveguide taper (VPC device input/output) is centered into the waveguide VNA ports with the assistance of a magnifying lens for aligning the 3-axes. A photograph of the experiment setup

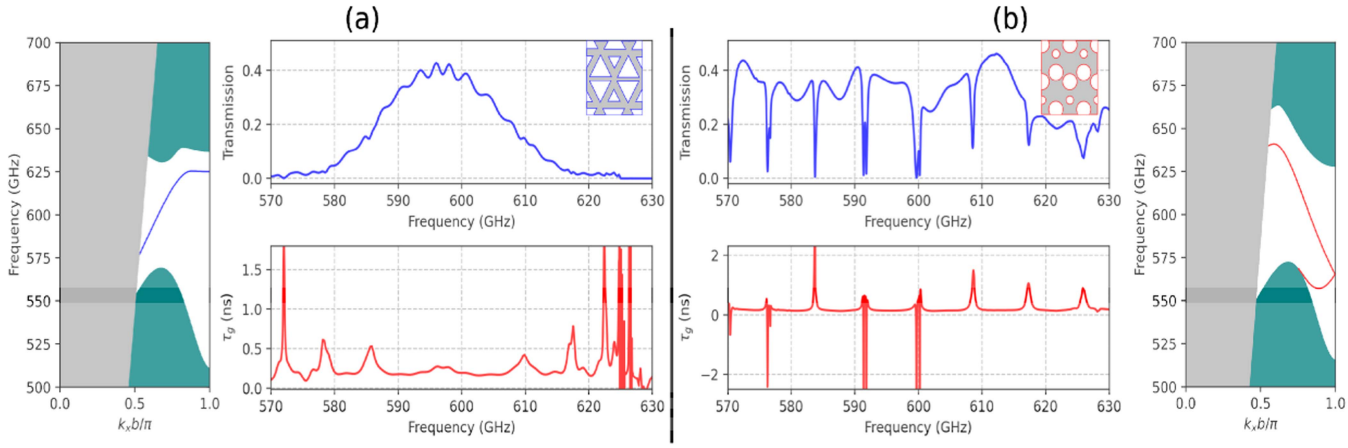

Fig. 6. Band diagrams, transmission spectra (top) and group delay (bottom) computed through the full 3D devices with single-cavity resonators, for triangular holes and zig-zag interface (a), and circular holes and bearded interface (b). In each case, the band diagram of the interface is plotted, with the light cone in grey and lattice bulk modes in blue-green.

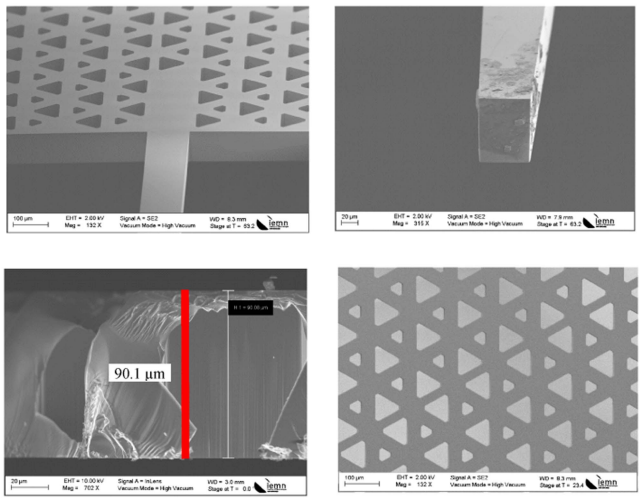

Fig. 7. SEM Images of VPC device with triangular air holes. The VPC device layer is 90μm after fabrication (HR-SI) and is symmetric in the z-direction.

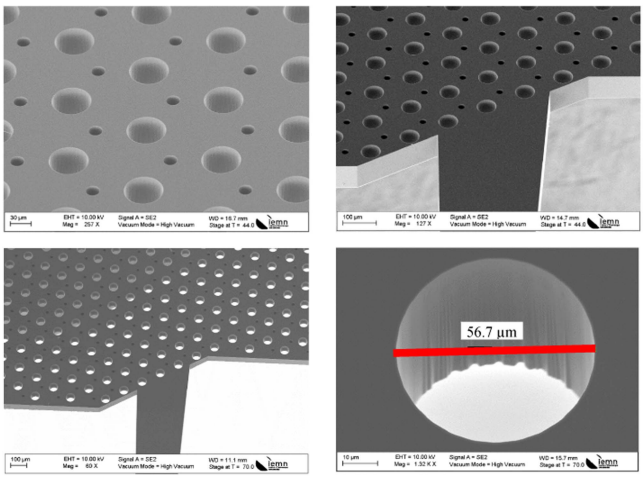

Fig. 8. SEM Images of VPC device with circular air holes.

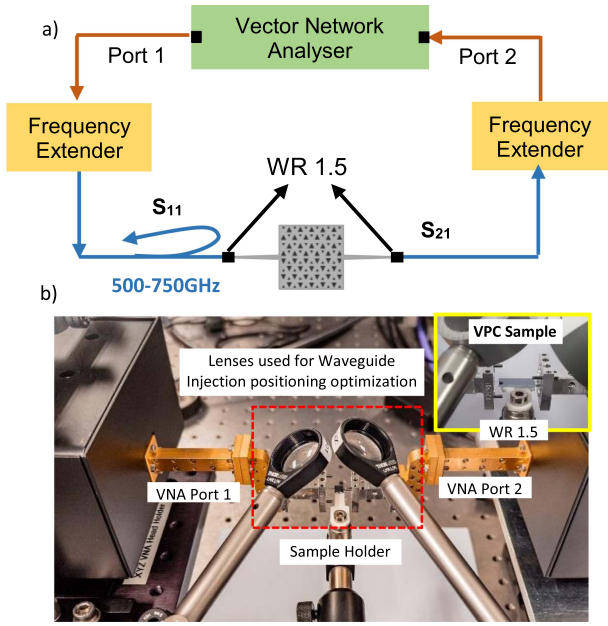

Fig. 9. (a) Block diagram representation of experimental setup for VNA characterization (b) The view showing the experiment setup during the VNA measurement of the devices. Waveguide (WR1.5) probes are connected to the VNA port as seen in the center-left and right. (Inset) The magnifying lens helps in the centering of the VPC taper in the waveguide probe.

during the VNA measurement of the VPC devices is shown in Fig. 9.

At this stage, the bending losses were not measured in these samples, as per the fabricated and available devices. However, the bending losses were discussed at 1.55 μm in [76].

C. Transmission and Group Delay, Triangular Holes

The measured S_{21} transmission and group delay for the devices are shown in the Fig. 10, for both THz topological ring resonator designs with zigzag and bearded interface using triangular holes. As the vector network analyzer is able to measure

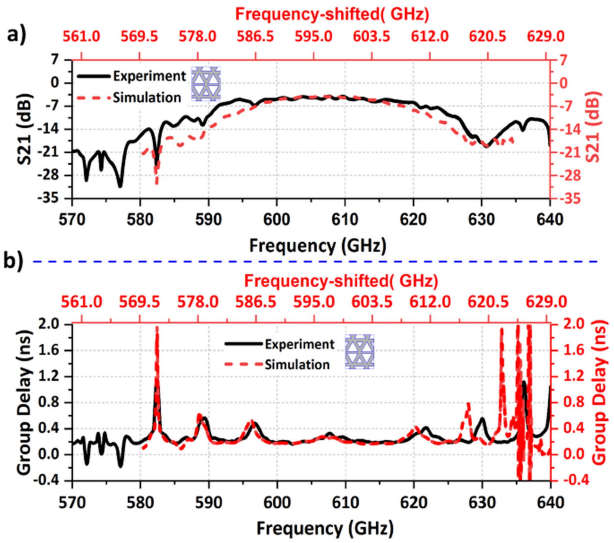

Fig. 10. (a) Transmission (black) from Vector Network Analyzer (VNA) measurement and simulation (red) for THz topological ring resonator fabricated using triangle holes and zigzag interface (b) Group delay from VNA measurement for the same design. The numerical bandgap is [568, 632] GHz (triangular holes).

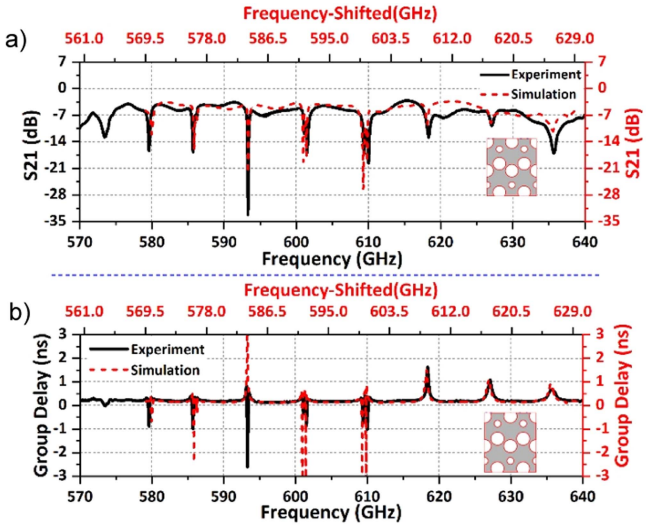

Fig. 11. (a) Transmission (black) from VNA measurement and simulation (red) for THz topological ring resonator fabricated using VPC design with the bearded interface and circular holes (b) Group delay from VNA measurement. The bandgap is [572629] GHz for circular holes.

the amplitude and phase of the S-parameters, the group-delay is calculated form $(-d\varphi)/d\omega$.

The transmission and group delay curves in all cases include simulation curves, which have been aligned with experimental curves by plotting them with a constant 10 GHz frequency shift. Fig. 10. displays the frequency-shifted x-axis at the top (red axis).

The S_{21} transmission exhibits sharp dips (peaks) at 582.38 GHz and several broader dips with relatively low Q factor. The smooths profile of the S_{21} over the 590–610 GHz range implies that this design provides relatively high topological protection and resilience toward backscattering at the corners. The computed group delay from complex phase data measured on VNA for these devices is shown in Fig. 10(b). A peak of 1.5 ns is spotted corresponding to the dip of 582.38 GHz in the transmission spectrum. Other small peaks are revealed in this measurement at frequencies corresponding to the eigenfrequencies of the topological cavity. The data shows low dispersion in the 600-620 GHz spectrum, confirmed by simulation Fig. 6(a), while group delay remains quite flat within the 590–610 GHz range. Despite a 10 GHz low-frequency shift, the numerical and experimental results align well. This means that the fabrication imperfections are negligible and the observed resonances arise from the triangular hole geometry. The average value of time delay in the central frequency of the spectrum center at 610 GHz is 0.25 ns. The relatively low dispersion in the central part of the frequency spectrum is due to the topological protection scaled up by the VPC design.

D. Transmission and Group Delay, Circular Holes

We now study triangular resonator fabricated using circular holes with bearded domain interfaces. Fig. 11(a) shows several sharp transmission dips at specific frequencies which include

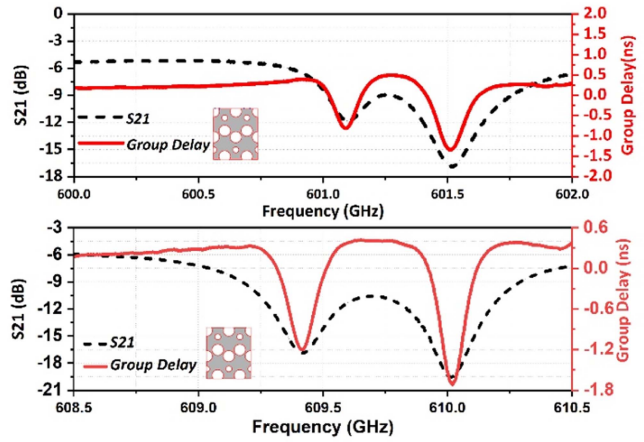

Fig. 12. Transmission and group delay for the Double peaks at 601 GHz and at 610 GHz from VNA measurement for THz triangular ring resonator with bearded interface and circular holes.

573.4, 579.64, 593.36, 601, 610, and 618.2 GHz. Notably, the transmission dip at 593.36 GHz exhibits a Q factor of approximately 34900. The observed double peaks at 601 and 610 GHz are a result of backscattering at the corners of the triangular resonator, displayed in more detail in the Figs. 12(a) and 8(b). The frequency difference between the two splits in the double peaks is $\Delta F' = 0.43$ GHz for the peaks at 601 GHz, and $\Delta F'' = 0.6$ GHz for the peaks at 610 GHz.

The measured S_{21} transmission and group delay for the devices are shown in the Fig. 11, for both THz topological ring resonator designs with zigzag and bearded interface using circular holes design. The double peaks are accurately replicated in the simulated data, perfectly matching the experimental verification, except for the constant 10 GHz low-frequency shift and

TABLE III
Q FACTOR CALCULATION FOR PEAKS OF THE RESONATOR WITH ROUND HOLES AND BEARDED INTERFACE

F_0 (GHz)	FWHM (GHz)	Q factor
585.702	0.13	4505
593.31	0.017	34 900
601.516	0.16	3844
610.016	0.134	4552
618.357	0.472	1353
627.095	0.86	729.1

for the resonance at 593 GHz which shows negative τ_g in the experiment but positive τ_g in the simulation.

We now discuss the origin of these two discrepancies. The constant low-frequency shift of about 10 GHz between the numerical results and the experiments can be attributed to small differences in the membrane thickness, silicon dielectric constant, but most probably to the simulation mesh, whose size has to be limited by the resources needed for those simulations (about 10^7 degrees of freedom, a typical RAM of 180GB and between 5 to 10 days of computation for one spectrum). Despite this constraint, the number and shape of the peaks is well reproduced, together with the frequency evolution of the group delay τ_g, whose values are almost the same as in the experiments.

The Free Spectral Range (FSR), which is the frequency spacing between two adjacent resonances, is a crucial parameter in the design of such resonators. The FSR of approximately 8 GHz is calculated for the dips in the central part of the spectral window which is also the case in simulated spectrum. The central part of the spectrum displays a sharp negative delay of -2.6 ns corresponding to the high Q factor dip at 593.36 GHz. The double delay peaks at 601 and 610 GHz frequencies are also refined from the simulation. The overall group delay in the transmission regions without peaks closely approaches zero as on Fig. 11(b), aligning with the simulation data where zero delay is also observed. By utilizing a bearded interface and circular air holes combination in the THz topological ring resonator can achieve high Q factor peaks through the downscaling of topological protection. This design is well-suite for highly compact and efficient sensors, optical switches, filters, modulators, and quantum information processing due to its ability to provide narrow peaks with a high Q factor. Thus, we can confirm that scaling down topological protection as a parameter enhances the Q factor, making it advantageous for sensing and filtering applications.

The measured negative delay of -2.6 ns corresponding to the high Q factor dip at 593.36 GHz is not present in the simulation. The reason is that experimental imperfections make that resonance very deep (see Fig. 11(a)), with a high amount of energy stored. Part of it leaks out through the sides of the device.

The Q factors for the resonance peaks of the two cavities are presented in Tables III and IV. The calculation of the Q factor of a resonant peak using the Full Width at Half Minimum (FWHM), is done in 3 steps. First, the resonance frequency (F_0), is identified. Next, the FWHM of the peak, which is the width of the peak at half of its minimum amplitude is evaluated. Finally, the Q factor is calculated using $Q = F_0/\Delta F$, where ΔF is the FWHM. This method provides a measure of the sharpness of the resonance. Here, no fano resonance curve fitting was done since most of the peaks we extracted were symmetric and compatible to find the Q factor and linewidth using the above-mentioned method.

TABLE IV
Q FACTOR CALCULATION FOR PEAKS OF THE RESONATOR WITH TRIANGULAR HOLES AND ZIGZAG INTERFACE

F_0 (GHz)	FWHM (GHz)	Q factor
572.106	0.372	1537.9
582.528	0.269	2169
589.271	13	44.9
596.687	3.1	192

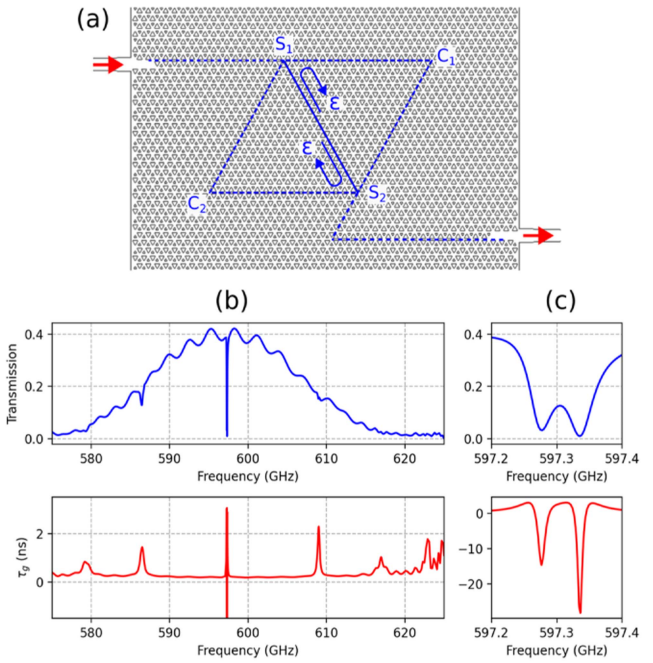

Fig. 13. (a) Top view of the device with double-cavity resonator. Corners are labelled C_1 and C_2, splitters S_1 and S_2. The parameter ε is the reflection coefficient on the splitter, for an edge mode propagating along the common edge S_1S_2 of the double cavity. (b) Transmission spectra (top) and group delay (bottom) as a function of the frequency; (c) same as (b) for a frequency range closer to the split resonance at 597 GHz.

Over all we seen that by utilizing a bearded interface and circular air holes in the ring resonator, we can implement high Q factor peaks through the downscaling of topological protection. This design is well-suited for highly compact and efficient sensors, optical switches, filters, modulators, and quantum information processing due to its ability to provide narrow peaks with a high Q factor. Thus, we can confirm that scaling down topological protection as a parameter enhances the Q factor, making it advantageous for sensing and filtering applications.

V. THz Topological Double Cavity

Fig. 13(a) shows the double cavity structure, created using the addition of 2 single cavity with 60° bends, which was fixed as

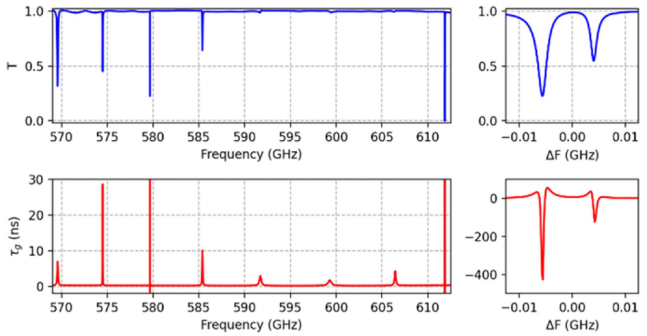

Fig. 14. Transmission and group delay for the bidimensional double-cavity resonator. For the zoom on the split resonance at 579 GHz (right panels), $\Delta F = F\text{-}F_0$, and $F_0 = 579.6825$ GHz.

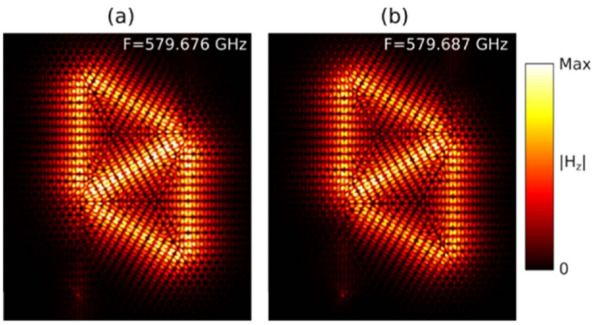

Fig. 15. Magnetic field distributions corresponding to the split-resonance of Fig. 14.

before from the VPC design. Fig. 13(b) and (c) shows the 3D simulated transmission spectrum and group delay of a double-cavity resonator, where two triangular cavities are united along a common zigzag edge, using photonic crystal made of triangular holes, see Fig. 13(a). This simulation is to be compared to the single cavity case on case with the same type of holes and interface displayed in Fig. 6(a).

Two transmission features are visible on the double-cavity spectrum, Fig. 13(b): a first shallow minimum close to F = 587 GHz, and a very sharp split-resonance at 597.3 GHz, whose detailed profile is seen for a reduced frequency window on Fig. 13(c). The frequency interval between both transmission minima is $\Delta F' = 60$ MHz, which is lower by a factor of about 8 than the value obtained for the split resonances of the single cavities with circular holes and bearded edge. In order to interpret this resonance, we first notice that it cannot be related to back-scattering at the two corners (C_1 and C_2), as otherwise double peaks would be observed in the single cavity simulations. For this reason, it must be attributed to backscattering occurring at both splitters (S_1 and S_2), for example along the edge S_1S_2.

Using the same method in [46], we can estimate the amplitude of the corresponding backscattering coefficient ε to be $|\varepsilon|^2 = 0.014\%$ in power. As for the single cavity, the fact that the group velocity reaches negative values (down to –28 ns) is attributed to the leakage in air at the edge of the device. For comparison, the simulation of the bi-dimensional case is given in Fig. 14.

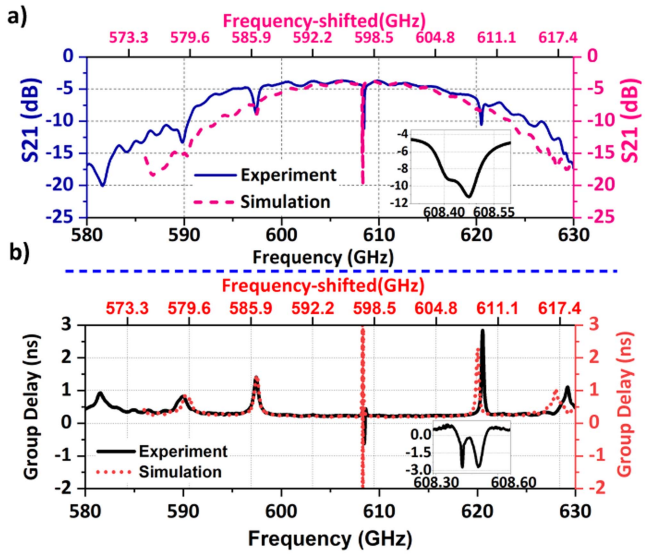

Fig. 16. (a) Transmission from VNA measurement for the topological double cavity resonator. Inset shows the double peak at 608 GHz (b) Group delay from VNA measurement for the topological double cavity resonator. Inset shows the double peak at 608 GHz.

The Fig. 15 shows the magnetic field distributions corresponding to the split resonance shown in Fig. 14.

In these simulations, both split-resonances show negative group delay. The origin is the same as above: the peaks are very narrow and the enhancement of the magnetic field inside the cavity is very large. As a consequence, the cavity mode leaks in the PMLs. For a sufficiently large simulation domain (but which could not be reached numerically), the transmission should become zero, and the group delay is positive. Fig. 10 shows the experimental validation of the double cavity device. Again, the comparison with the experiment shown in Fig. 16(a) is very good, despite the frequency shift of about 10.2 GHz. However, the width of the peaks of the split-resonances is larger in the experimental transmission. The reason is that the two underlying peaks overlap: the lowest-frequency peak appears as a shoulder of the high-frequency peak, but the frequency interval is consistent with simulations.

Similarly, the experimental group delay is in good agreement for the single peak resonances but strongly differs in amplitude for the double peak, where it reaches about –2.7 ns. Those differences are the signature of additional losses in the experimental device, which could be attributed to the small in homogeneities of the shape of holes, or to a lower resistivity of the silicon, which was not taken into account in the simulations.

VI. Conclusion

This work provides perspectives to use the degree of topological protection as a knob to scale passive functions of photonic crystal designs. Here the VPCs with the zigzag interface and triangular air holes provide more robust topological protection to the edge modes while the bearded interface with circular air holes relaxes the protection. Interestingly, the downgraded topological protection of triangular topological cavities made of

circular air-holes with bearded interfaces can be used to engineer high Q factor resonances in the cavity design, which is of potential use for filtering and sensing applications. This work is also proposing first experimental validation of passive functional for the 600 GHz band, providing valuable pathways towards high speed 6G data communication Technology building blocks [77].

REFERENCES

[1] M. I. Shalaev, W. Walasik, A. Tsukernik, Y. Xu, and N. M. Litchinitser, "Robust topologically protected transport in photonic crystals at telecommunication wavelengths," *Nature Nanotechnol.*, vol. 14, no. 1, pp. 31–34, Jan. 2019, doi: 10.1038/s41565-018-0297-6.

[2] Z. Wang, Y. Chong, J. D. Joannopoulos, and M. Soljacić, "Observation of unidirectional backscattering-immune topological electromagnetic states," *Nature*, vol. 461, no. 7265, pp. 772–775, Oct. 2009, doi: 10.1038/nature08293.

[3] X.-T. He et al., "A silicon-on-insulator slab for topological valley transport," *Nature Commun.*, vol. 10, no. 1, Feb. 2019, Art. no. 872, doi: 10.1038/s41467-019-08881-z.

[4] A. B. Khanikaev and G. Shvets, "Two-dimensional topological photonics," *Nature Photon.*, vol. 11, no. 12, pp. 763–773, Dec. 2017, doi: 10.1038/s41566-017-0048-5.

[5] L. Lu, J. D. Joannopoulos, and M. Soljačić, "Topological photonics," *Nature Photon.*, vol. 8, no. 11, pp. 821–829, Nov. 2014, doi: 10.1038/nphoton.2014.248.

[6] M. He, L. Zhang, and H. Wang, "Two-dimensional photonic crystal with ring degeneracy and its topological protected edge states," *Sci. Rep.*, vol. 9, no. 1, Mar. 2019, Art. no. 3815, doi: 10.1038/s41598-019-40677-5.

[7] S. Mallick, N. Chourasia, R. Singh, and D. Roy Chowdhury, "Demonstration of toroidal metasurfaces through near-field coupling of bright-mode resonators," *Appl. Phys. Exp.*, vol. 15, no. 1, Jan. 2022, Art. no. 012005, doi: 10.35848/1882-0786/ac38b0.

[8] C. Liu, M. V. Rybin, P. Mao, S. Zhang, and Y. Kivshar, "Disorder-Immune photonics based on mie-resonant dielectric metamaterials," *Phys. Rev. Lett.*, vol. 123, no. 16, Oct. 2019, Art. no. 163901, doi: 10.1103/PhysRevLett.123.163901.

[9] A. A. Burkov and L. Balents, "Weyl Semimetal in a topological insulator multilayer," *Phys. Rev. Lett.*, vol. 107, no. 12, Sep. 2011, Art. no. 127205, doi: 10.1103/PhysRevLett.107.127205.

[10] D. Smirnova, D. Leykam, Y. Chong, and Y. Kivshar, "Nonlinear topological photonics," *Appl. Phys. Rev.*, vol. 7, no. 2, Jun. 2020, Art. no. 021306, doi: 10.1063/1.5142397.

[11] L. J. Maczewsky et al., "Nonlinearity-induced photonic topological insulator," *Science*, vol. 370, no. 6517, pp. 701–704, Nov. 2020, doi: 10.1126/science.abd2033.

[12] Z. Wang, Y. D. Chong, J. D. Joannopoulos, and M. Soljačić, "Reflection-free one-way edge modes in a gyromagnetic photonic crystal," *Phys. Rev. Lett.*, vol. 100, no. 1, Jan. 2008, Art. no. 013905, doi: 10.1103/PhysRevLett.100.013905.

[13] K. Klitzing, G. Dorda, and M. Pepper, "New method for high-accuracy determination of the fine-structure constant based on quantized hall resistance," *Phys. Rev. Lett.*, vol. 45, no. 6, pp. 494–497, Aug. 1980, doi: 10.1103/PhysRevLett.45.494.

[14] X.-L. Qi and S.-C. Zhang, "The quantum spin Hall effect and topological insulators," *Phys. Today*, vol. 63, no. 1, pp. 33–38, Jan. 2010, doi: 10.1063/1.3293411.

[15] J.-W. Dong, X.-D. Chen, H. Zhu, Y. Wang, and X. Zhang, "Valley photonic crystals for control of spin and topology," *Nature Mater*, vol. 16, no. 3, pp. 298–302, Mar. 2017, doi: 10.1038/nmat4807.

[16] M. Tahir, A. Manchon, K. Sabeeh, and U. Schwingenschlögl, "Quantum spin/valley Hall effect and topological insulator phase transitions in silicene," *Appl. Phys. Lett.*, vol. 102, no. 16, Apr. 2013, Art. no. 162412, doi: 10.1063/1.4803084.

[17] X. Wu et al., "Direct observation of valley-polarized topological edge states in designer surface plasmon crystals," *Nature Commun.*, vol. 8, no. 1, Nov. 2017, Art. no. 1304, doi: 10.1038/s41467-017-01515-2.

[18] M. Hafezi, S. Mittal, J. Fan, A. Migdall, and J. M. Taylor, "Imaging topological edge states in silicon photonics," *Nature Photon.*, vol. 7, no. 12, pp. 1001–1005, Dec. 2013, doi: 10.1038/nphoton.2013.274.

[19] W.-J. Chen et al., "Experimental realization of photonic topological insulator in a uniaxial metacrystal waveguide," *Nature Commun.*, vol. 5, no. 1, Dec. 2014, Art. no. 5782, doi: 10.1038/ncomms6782.

[20] L.-H. Wu and X. Hu, "Scheme for achieving a topological photonic crystal by using dielectric material," *Phys. Rev. Lett.*, vol. 114, no. 22, Jun. 2015, Art. no. 223901, doi: 10.1103/PhysRevLett.114.223901.

[21] X. Cheng, C. Jouvaud, X. Ni, S. H. Mousavi, A. Z. Genack, and A. B. Khanikaev, "Robust reconfigurable electromagnetic pathways within a photonic topological insulator," *Nature Mater.*, vol. 15, no. 5, pp. 542–548, May 2016, doi: 10.1038/nmat4573.

[22] S. Yves, R. Fleury, T. Berthelot, M. Fink, F. Lemoult, and G. Lerosey, "Crystalline metamaterials for topological properties at subwavelength scales," *Nature Commun.*, vol. 8, no. 1, Jul. 2017, Art. no. 16023, doi: 10.1038/ncomms16023.

[23] F. Gao et al., "Topologically protected refraction of robust kink states in valley photonic crystals," *Nature Phys.*, vol. 14, no. 2, pp. 140–144, Feb. 2018, doi: 10.1038/nphys4304.

[24] J. Noh, S. Huang, K. P. Chen, and M. C. Rechtsman, "Observation of photonic topological Valley Hall edge states," *Phys. Rev. Lett.*, vol. 120, no. 6, Feb. 2018, Art. no. 063902, doi: 10.1103/PhysRevLett.120.063902.

[25] S. Barik et al., "A topological quantum optics interface," *Science*, vol. 359, no. 6376, pp. 666–668, Feb. 2018, doi: 10.1126/science.aaq0327.

[26] S. Mittal, E. A. Goldschmidt, and M. Hafezi, "A topological source of quantum light," *Nature*, vol. 561, pp. 502–506, Sep. 2018, doi: 10.1038/s41586-018-0478-3.

[27] Y. Zeng et al., "Electrically pumped topological laser with valley edge modes," *Nature*, vol. 578, no. 7794, pp. 246–250, Feb. 2020, doi: 10.1038/s41586-020-1981-x.

[28] A. Dikopoltsev et al., "Topological insulator vertical-cavity laser array," *Science*, vol. 373, no. 6562, pp. 1514–1517, Sep. 2021, doi: 10.1126/science.abj2232.

[29] M. Hafezi, E. A. Demler, M. D. Lukin, and J. M. Taylor, "Robust optical delay lines with topological protection," *Nature Phys.*, vol. 7, no. 11, pp. 907–912, Nov. 2011, doi: 10.1038/nphys2063.

[30] W.-J. Chen et al., "Experimental realization of photonic topological insulator in a uniaxial metacrystal waveguide," *Nature Commun.*, vol. 5, no. 1, Dec. 2014, Art. no. 5782, doi: 10.1038/ncomms6782.

[31] Y. Lu and X. Zheng, "6G: A survey on technologies, scenarios, challenges, and the related issues," *J. Ind. Inf. Integration*, vol. 19, Sep. 2020, Art. no. 100158, doi: 10.1016/j.jii.2020.100158.

[32] P. Hillger, J. Grzyb, R. Jain, and U. R. Pfeiffer, "Terahertz imaging and sensing applications with silicon-based technologies," *IEEE Trans. THz Sci. Technol.*, vol. 9, no. 1, pp. 1–19, Jan. 2019, doi: 10.1109/TTHZ.2018.2884852.

[33] M. Tonouchi, "Cutting-edge terahertz technology," *Nature Photon.*, vol. 1, no. 2, pp. 97–105, Feb. 2007, doi: 10.1038/nphoton.2007.3.

[34] P. H. Siegel, "Terahertz technology in biology and medicine," *IEEE Trans. Microw. Theory Techn.*, vol. 52, no. 10, pp. 2438–2447, Oct. 2004, doi: 10.1109/TMTT.2004.835916.

[35] S. Dang, O. Amin, B. Shihada, and M.-S. Alouini, "What should 6G be?," *Nature Electron.*, vol. 3, no. 1, pp. 20–29, Jan. 2020, doi: 10.1038/s41928-019-0355-6.

[36] Q. J. Gu, "THz interconnect: The last centimeter communication," *IEEE Commun. Mag.*, vol. 53, no. 4, pp. 206–215, Apr. 2015, doi: 10.1109/MCOM.2015.7081096.

[37] D. J. Harris, "Waveguides for the 100-1000 GHz frequency range," *Radio Electron. Engineer*, vol. 49, pp. 389–394, Aug. 1979.

[38] G. Gallot, S. P. Jamison, R. W. McGowan, and D. Grischkowsky, "Terahertz waveguides," *J. Opt. Soc. Amer. B*, vol. 17, no. 5, May 2000, Art. no. 851, doi: 10.1364/JOSAB.17.000851.

[39] I. F. Akyildiz, A. Kak, and S. Nie, "6G and beyond: The future of wireless communications systems," *IEEE Access*, vol. 8, pp. 133995–134030, 2020, doi: 10.1109/ACCESS.2020.3010896.

[40] Y. Yang et al., "Terahertz topological photonics for on-chip communication," *Nature Photon.*, vol. 14, no. 7, pp. 446–451, Jul. 2020, doi: 10.1038/s41566-020-0618-9.

[41] J. Webber et al., "Terahertz band communications with topological valley photonic crystal waveguide," *J. Lightw. Technol.*, vol. 39, no. 24, pp. 7609–7620, Dec. 2021.

[42] K. M. Devi, S. Jana, and D. R. Chowdhury, "Topological edge states in an all-dielectric terahertz photonic crystal," *Opt. Mater. Exp.*, vol. 11, no. 8, pp. 2445–2458, Aug. 2021, doi: 10.1364/OME.427069.

[43] S. Jana, K. M. Devi, and D. R. Chowdhury, "Effect of asymmetry on terahertz transmissions in topological photonic crystals comprising of dielectric rod structures," *Opt. Commun.*, vol. 505, Feb. 2022, Art. no. 127589, doi: 10.1016/j.optcom.2021.127589.

[44] Y. J. Tan, W. Wang, A. Kumar, and R. Singh, "Interfacial topological photonics: Broadband silicon waveguides for THz 6G communication and beyond," *Opt. Exp.*, vol. 30, no. 18, Aug. 2022, Art. no. 33035, doi: 10.1364/OE.468010.

[45] W.-S. Ruan, X.-T. He, F.-L. Zhao, and J.-W. Dong, "Analysis of unidirectional coupling in topological valley photonic crystal waveguides," *J. Lightw. Technol.*, vol. 39, no. 4, pp. 889–895, Feb. 2021, doi: 10.1109/JLT.2020.3024696.

[46] G. Lévêque, Y. Pennec, P. Szriftgiser, A. Amo, and A. Martínez, "Scattering-matrix approach for a quantitative evaluation of the topological protection in valley photonic crystals," *Phys. Rev. A*, vol. 108, 2023, Art. no. 043505, doi: 10.48550/ARXIV.2301.10565.

[47] W. Bogaerts et al., "Silicon microring resonators," *Laser Photon. Rev.*, vol. 6, no. 1, pp. 47–73, 2012, doi: 10.1002/lpor.201100017.

[48] E. Sauer, J. P. Vasco, and S. Hughes, "Theory of intrinsic propagation losses in topological edge states of planar photonic crystals," *Phys. Rev. Res.*, vol. 2, no. 4, Oct. 2020, Art. no. 043109, doi: 10.1103/PhysRevResearch.2.043109.

[49] P. D. Anderson and G. Subramania, "Unidirectional edge states in topological honeycomb-lattice membrane photonic crystals," *Opt. Exp.*, vol. 25, no. 19, Sep. 2017, Art. no. 23293, doi: 10.1364/OE.25.023293.

[50] J. Noh et al., "Topological protection of photonic mid-gap defect modes," *Nature Photon.*, vol. 12, no. 7, pp. 408–415, Jul. 2018, doi: 10.1038/s41566-018-0179-3.

[51] X. Liu, L. Zhao, D. Zhang, and S. Gao, "Topological cavity laser with valley edge states," *Opt. Exp.*, vol. 30, no. 4, pp. 4965–4977, Feb. 2022, doi: 10.1364/OE.450558.

[52] L. Gu et al., "A topological photonic ring-resonator for on-chip channel filters," *J. Lightw. Technol.*, vol. 39, no. 15, pp. 5069–5073, Aug. 2021, doi: 10.1109/JLT.2021.3082558.

[53] M. J. Mehrabad et al., "A semiconductor topological photonic ring resonator," *Appl. Phys. Lett.*, vol. 116, no. 6, Feb. 2020, Art. no. 061102, doi: 10.1063/1.5131846.

[54] M. Wu et al., "On-chip ultra-compact hexagonal boron nitride topological ring-resonator in visible region," *J. Lightw. Technol.*, vol. 40, no. 23, pp. 7610–7618, Dec. 2022, doi: 10.1109/JLT.2022.3203563.

[55] A. Kumar et al., "Active ultrahigh- Q (0.2×10^6) THz topological cavities on a chip," *Adv. Mater.*, vol. 34, no. 27, Jul. 2022, Art. no. 2202370, doi: 10.1002/adma.202202370.

[56] S. Barik, A. Karasahin, S. Mittal, E. Waks, and M. Hafezi, "Chiral quantum optics using a topological resonator," *Phys. Rev. B*, vol. 101, no. 20, May 2020, Art. no. 205303, doi: 10.1103/PhysRevB.101.205303.

[57] Z. Wang, G. Dong, S. Yuan, L. Chen, X. Wu, and X. Zhang, "Voltage-actuated thermally tunable on-chip terahertz filters based on a whispering gallery mode resonator," *Opt. Lett.*, vol. 44, no. 19, pp. 4670–4673, Oct. 2019, doi: 10.1364/OL.44.004670.

[58] C. M. Yee and M. S. Sherwin, "High-Q terahertz microcavities in silicon photonic crystal slabs," *Appl. Phys. Lett.*, vol. 94, no. 15, Apr. 2009, Art. no. 154104, doi: 10.1063/1.3118579.

[59] B. Jalali and S. Fathpour, "Silicon photonics," *J. Lightw. Technol.*, vol. 24, no. 12, pp. 4600–4615, Dec. 2006.

[60] R. Soref, "The past, present, and future of Silicon photonics," *IEEE J. Sel. Topics Quantum Electron.*, vol. 12, no. 6, pp. 1678–1687, Nov. 2006, doi: 10.1109/JSTQE.2006.883151.

[61] W. Withayachumnankul, M. Fujita, and T. Nagatsuma, "Integrated silicon photonic crystals toward terahertz communications," *Adv. Opt. Mater.*, vol. 6, no. 16, 2018, Art. no. 1800401.

[62] S. Y. Siew et al., "Review of Silicon Photonics technology and Platform development," *J. Lightw. Technol.*, vol. 39, no. 13, pp. 4374–4389, Jul. 2021, doi: 10.1109/JLT.2021.3066203.

[63] D. Thomson et al., "Roadmap on silicon photonics," *J. Opt.*, vol. 18, no. 7, Jun. 2016, Art. no. 073003, doi: 10.1088/2040-8978/18/7/073003.

[64] H. J. Caulfield and S. Dolev, "Why future supercomputing requires optics," *Nature Photon.*, vol. 4, no. 5, pp. 261–263, May 2010, doi: 10.1038/nphoton.2010.94.

[65] S. Jana, K. M. Devi, and D. R. Chowdhury, "Role of unit-cell defects in terahertz topological ring resonators," *J. Opt. Soc. Amer. B*, vol. 39, no. 6, Jun. 2022, Art. no. 1590, doi: 10.1364/JOSAB.453115.

[66] A. Kumar et al., "Phototunable chip-scale topological photonics: 160 Gbps waveguide and demultiplexer for THz 6G communication," *Nature Commun.*, vol. 13, no. 1, Sep. 2022, Art. no. 5404, doi: 10.1038/s41467-022-32909-6.

[67] Y. Sun et al., "The perspective of topological photonics for on-chip terahertz modulation and sensing," *APL Photon.*, vol. 8, no. 11, 2023, Art. no. 110901.

[68] A. Kumar et al., "Slow light topological photonics with counter-propagating waves and its active control on a chip," *Nature Commun.*, vol. 15, 2024, Art. no. 926, doi: 10.1038/s41467-024-45175-5.

[69] R. Banerjee et al., "On-chip amorphous THz topological photonic interconnects," 2023, *arXiv:2311.05576*.

[70] R. Kumar et al., "Valley-conserved topological integrated antenna for 100-Gbps THz 6G wireless," *Sci. Adv.*, vol. 9, no. 44, 2023, Art. no. eadi8500.

[71] M. Gupta, N. Navaratna, P. Szriftgiser, G. Ducournau, and R. Singh, "327 Gbps THz silicon photonic interconnect with sub-λ bends," *Appl. Phys. Lett.*, vol. 123, no. 17, 2023, Art. no. 171102.

[72] M. Gupta, A. Kumar, and R. Singh, "Electrically tunable topological notch filter for THz integrated photonics," *Adv. Opt. Mater.*, vol. 11, no. 23, 2023, Art. no. 2301051.

[73] A. Kumar, M. Gupta, and R. Singh, "Topological integrated circuits for 5G and 6G," *Nature Electron.*, vol. 5, pp. 261–262, 2022, doi: 10.1038/s41928-022-00775-1.

[74] N. Navaratna, Y. J. Tan, A. Kumar, M. Gupta, and R. Singh, "On-chip topological THz biosensors," *Appl. Phys. Lett.*, vol. 123, no. 3, 2023, Art. no. 033705.

[75] E. Akiki et al., "High-Q THz photonic crystal cavity on a low-loss suspended silicon platform," *IEEE Trans. THz Sci. Technol.*, vol. 11, no. 1, pp. 42–53, Jan. 2021, doi: 10.1109/TTHZ.2020.3019928.

[76] S. Arora et al., "Direct quantification of topological protection in symmetry-protected photonic edge states at telecom wavelengths," *Light Sci. Appl.*, vol. 10, 2021, Art. no. 9, doi: 10.1038/s41377-020-00458-6.

[77] A. S. Mohammed et al., "120 Gbit/s Aggregated Channel Transmission in the 600 GHz Band Using Topological Waveguide,". in *Proc. 54th Eur. Microw. Conf.*, Paris, France, 2024.